A. Datasets Description

ACDC (2018) [1]: Automated Cardiac Diagnosis Challenge dataset containing 150 cardiac MRI scans from different patients with multi-structure segmentation annotations for left ventricle, right ventricle, and myocardium. Acquired over 6 years at University Hospital of Dijon using 1.5T and 3.0T Siemens scanners with SSFP sequences, spatial resolution 1.37-1.68 mm²/pixel, slice thickness 5-8mm, and 28-40 cardiac cycle frames. Dataset encompasses five evenly distributed groups (30 patients each): healthy subjects and four cardiac pathologies including dilated cardiomyopathy, hypertrophic cardiomyopathy, myocardial infarction, and abnormal right ventricle, representing comprehensive cardiac imaging scenarios for automated diagnosis assistance.

ABD-MRI (2021) [4]: CHAOS Challenge combined healthy abdominal organ segmentation dataset comprising 40 T2-SPIR weighted MRI scans (20 training cases) with annotations for liver, spleen, left kidney, and right kidney. Acquired using 1.5T Philips MRI producing 12-bit DICOM images at 256×256 resolution with variable slice thickness 5.5-9mm (average 7.84mm), in-plane spacing 1.36-1.89mm (average 1.61mm), and 26-50 slices per volume. Dataset emphasizes cross-modality segmentation challenges and healthy organ delineation from potential liver donors, supporting development of automated abdominal imaging analysis for clinical assessment and surgical planning.

ABD-CT (2015) [5]: MICCAI Multi-Atlas Labeling Beyond the Cranial Vault dataset containing 50 abdominal CT scans from colorectal cancer chemotherapy trials and ventral hernia studies with multi-organ segmentation masks. Acquired during portal venous contrast phase with variable volumes (512×512×85-198), field of view 280-650mm³, in-plane resolution 0.54-0.98mm², and slice thickness 2.5-5.0mm. Dataset includes clinical cases from patients with metastatic liver cancer or postoperative abdominal wall hernia, providing comprehensive coverage of abdominal imaging challenges encountered in routine clinical practice and radiological interpretation.

PH2 (2013) [6]: Dermoscopic image database for skin lesion research containing 200 high-resolution (768×560 pixels) 8-bit RGB images acquired at Hospital Pedro Hispano, Portugal using Tuebinger Mole Analyzer with 20× magnification under standardized conditions. Dataset includes 80 atypical nevus, 40 melanoma cases, and 80 common nevi with expert dermatologist annotations including lesion segmentation, clinical assessment, and dermoscopic criteria evaluation (colors, pigment network, dots/globules, streaks). Supporting automated melanoma detection and skin cancer screening applications in dermatological practice with comprehensive clinical and histological diagnosis metadata.

CVC-300 (2017) [8]: Endoscopic scene segmentation benchmark containing 60 colonoscopy images with polyp annotations extracted from colonoscopy video sequences. Dataset emphasizes endoluminal scene understanding including polyp detection, lumen segmentation, and specular highlight identification, essential for computer-aided diagnosis during colonoscopy procedures.

CHASE-DB1 (2012) [3]: Retinal vessel segmentation database comprising 28 fundus photography images with manual vessel annotations from two independent human experts. Dataset covers diverse retinal imaging conditions and vessel morphologies, supporting automated diabetic retinopathy screening and cardiovascular risk assessment through retinal vessel analysis.

Drishti-GS (2014) [7]: Glaucoma screening dataset containing 70 fundus images with optic nerve head and optic cup segmentation annotations. Dataset emphasizes glaucoma detection challenges including varying optic disc appearances, cup-to-disc ratios, and pathological conditions, enabling automated glaucoma screening and early detection systems.

DCA1 (2019) [2]: Coronary artery segmentation dataset comprising 134 X-ray angiography images with vessel annotations. Dataset addresses interventional cardiology challenges including complex vessel morphologies, overlapping structures, and contrast variations typical in coronary angiographic procedures, supporting automated vessel analysis for cardiac intervention planning.

B. Math Proof

B.1. EDT Initialization Analysis

We provide the mathematical foundation for our EDT-based initialization scheme, which ensures robust starting conditions for the subsequent geodesic refinement process.

Definition B.1 (EDT Edge Detection)**.** For a binary mask $\mathbf{M} \in \{0,1\}^{H\times W}$, the EDT initialization incorporates edge detection via Sobel operators. The gradient magnitude is computed as:

$$\|\nabla \mathbf{M}_{i,j}\|_2 = \sqrt{(\mathbf{K}_x * \mathbf{M})^2_{i,j} + (\mathbf{K}_y * \mathbf{M})^2_{i,j} + \epsilon} \tag{1}$$

where $\mathbf{K}_x = \begin{bmatrix} -1 & 0 & 1 \\ -2 & 0 & 2 \\ -1 & 0 & 1 \end{bmatrix}$ and $\mathbf{K}_y = \begin{bmatrix} -1 & -2 & -1 \\ 0 & 0 & 0 \\ 1 & 2 & 1 \end{bmatrix}$ are Sobel kernels.

The EDT initialization $\mathbf{G}^{(0)}_{i,j} = \text{EDT}(\mathbf{M})_{i,j}$ satisfies:

(i) **Boundary condition:** $\mathbf{G}^{(0)}_{i,j} = 0$ for all $(i,j) \in \partial\mathbf{M}$;

(ii) **Monotonicity:** $\mathbf{G}^{(0)}_{i,j} \le \mathbf{G}^{(0)}_{k,l}$ whenever $d((i,j), \partial\mathbf{M}) \le d((k,l), \partial\mathbf{M})$;

(iii) **Lipschitz continuity:** $|\mathbf{G}^{(0)}_{i,j} - \mathbf{G}^{(0)}_{k,l}| \le \|(i,j) - (k,l)\|_2$.

Lemma B.2 (Speed Function Bounds)**.** *The speed function* $\mathbf{F}_{i,j} = \frac{1}{1+\boldsymbol{\beta}\|\nabla \mathbf{M}_{i,j}\|_2}$ *satisfies:*

$$\frac{1}{1+5\|\nabla \mathbf{M}_{i,j}\|_2} \le \mathbf{F}_{i,j} \le \frac{1}{1+0.5\|\nabla \mathbf{M}_{i,j}\|_2} \tag{2}$$

for $\boldsymbol{\beta} \in [0.5, 5.0]$.

B.2. Geodesic Refinement Analysis

This section establishes the theoretical foundations for the iterative geodesic distance field refinement process.

Theorem B.3 (Geodesic Refinement Convergence)**.** *Let* $\mathcal{T} : \mathbb{R}^{H\times W} \to \mathbb{R}^{H\times W}$ *denote the geodesic refinement operator defined by:*

$$\mathbf{U}^{(t)}_{i,j} = \min_{(k,l)\in\mathcal{N}(i,j)} \mathbf{G}^{(t-1)}_{k,l} + \frac{\lambda}{\mathbf{F}_{i,j} + \epsilon}, \tag{3}$$

$$\mathbf{G}^{(t)}_{i,j} = \begin{cases} \mu\mathbf{G}^{(t-1)}_{i,j} + (1-\mu)\mathbf{U}^{(t)}_{i,j}, & \textit{if } \mathbf{M}_{i,j} > \tau, \\ \mathbf{G}^{(t-1)}_{i,j}, & \textit{otherwise}. \end{cases} \tag{4}$$

Then $\mathcal{T}$ *is a contraction mapping with Lipschitz constant* $\mu < 1$*, and the sequence* $\{\mathbf{G}^{(t)}\}_{t=0}^{\infty}$ *converges to a unique fixed point.*

Proof. The mixing parameter $\mu = 0.7$ in Eq. (4) ensures contractivity. For any two distance fields G_1, G_2:

$$\|T(G_1) - T(G_2)\|_2 \le \mu\|G_1 - G_2\|_2$$

Since $\mu < 1$, the Banach fixed-point theorem guarantees convergence.

Lemma B.4 (Numerical Stability)**.** *The numerical scheme in Eq.* (4) *is stable under the condition:*

$$\mu \le 1 - \frac{\lambda}{\min_{i,j} \mathbf{F}_{i,j}} \tag{5}$$

Given our parameter choices ($\mu = 0.7$*,* $\lambda = 0.1$*) and the speed function bounds from Lemma B.2, this condition is satisfied for all practical cases.*

Remark B.5. The regularization parameter $\epsilon = 10^{-6}$ in Eq. (3) ensures numerical stability by preventing division by zero while maintaining approximation accuracy to machine precision.

B.3. Prototype Space Analysis

We analyze the theoretical properties of our unified prototype representation that combines both local and global spatial information.

Definition B.6 (Unified Prototype Space)**.** The unified prototype space $\mathbf{P}_{\text{unified}} = \{\mathbf{P}_{grid}\} \cup \{\mathbf{p}_{\text{global}}\}$ forms a complete representation of the support features with both local and global information. Specifically:

(i) **Local prototypes:** $mathbf{P}_{grid}\}$ capture spatial heterogeneity through adaptive grid sampling with density $\rho_{i,j} = 1 + \sigma \cdot \tau \cdot \|\nabla \mathbf{G}_{i,j}\|_2$ where $\sigma \in [1.0, 4.0]$ and $\tau \in [0.5, 3.0]$;

(ii) **Global prototype:** $\mathbf{p}_{\text{global}}$ provides anatomical structure coherence via geodesic-weighted aggregation using Eq. **??**;

(iii) **Completeness:** The unified space spans both fine-grained boundary details and global anatomical patterns for comprehensive medical image representation.

Lemma B.7 (Adaptive Density Bounds)**.** *The adaptive sampling density* $\rho_{i,j} = 1 + \sigma \cdot \tau \cdot \|\nabla \mathbf{G}_{i,j}\|_2$ *with* $\sigma \in [1.0, 4.0]$ *and* $\tau \in [0.5, 3.0]$ *ensures:*

$$1 \leq \rho_{i,j} \leq 1 + 12 \max_{i,j} \|\nabla \mathbf{G}_{i,j}\|_2 \tag{6}$$

providing bounded density variation that concentrates sampling near boundaries.

Theorem B.8 (Prototype Bounds)**.** *Each grid prototype* $\mathbf{P}_{g,h}$ *computed via:*

$$\mathbf{P}_{grid} = \frac{\sum_{(i,j) \in \mathcal{N}_{g,h}} \rho_{i,j} \cdot w_{i,j} \cdot \mathbf{M}_{i,j} \cdot \mathbf{F}_{i,j}}{\sum_{(i,j) \in \mathcal{N}_{g,h}} \rho_{i,j} \cdot w_{i,j} \cdot \mathbf{M}_{i,j} + \epsilon} \tag{7}$$

satisfies:

$$\|\mathbf{P}_{grid}\|_2 \leq \max_{(i,j) \in \mathcal{N}_{g,h}} \|\mathbf{F}_{i,j}\|_2 \tag{8}$$

ensuring bounded prototype magnitudes.

Proof. The normalization in Eq. (7) ensures that $\mathbf{P}_{g,h}$ is a convex combination of feature vectors $\mathbf{F}_{i,j}$ within the neighborhood $\mathcal{N}_{g,h}$. The bound follows from the convexity of the ℓ_2 norm.

Corollary B.9 (Prototype Convergence). Under bounded feature assumptions, the prototype computation converges to a stable representation with finite norm.

C. Qualitative results

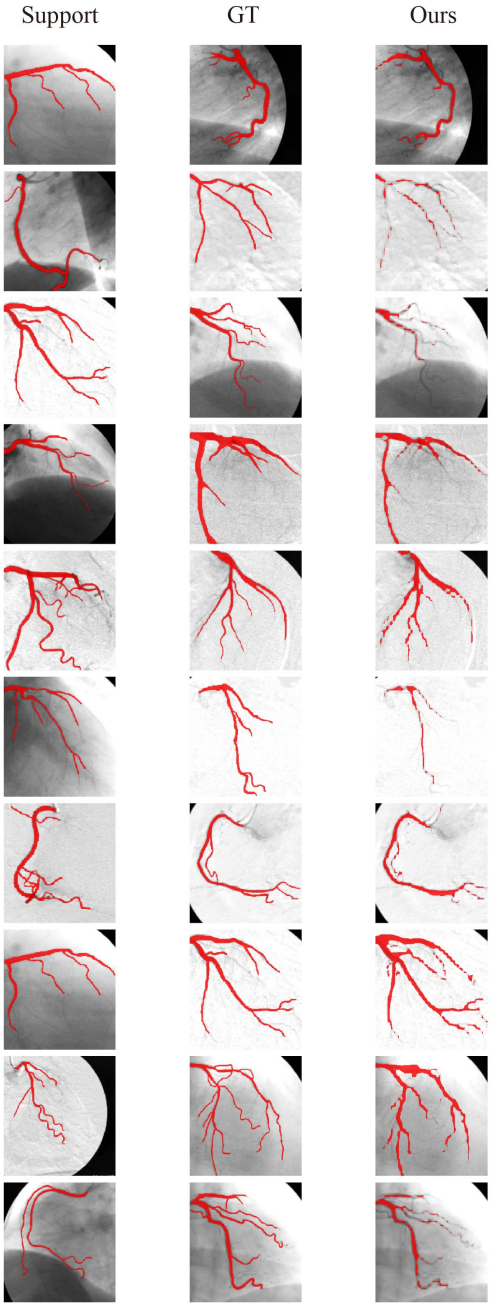

Figure 1. Visualization from left to right on DCA1 dataset. left row to right: Support, Ground-truth. Ours prediction.

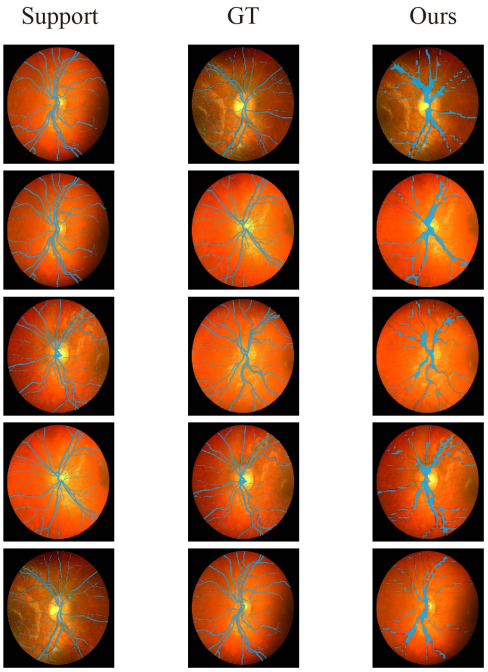

Figure 2. Visualization from left to right on CHASE-DB1 dataset. left row to right: Support, Ground-truth. Ours prediction.

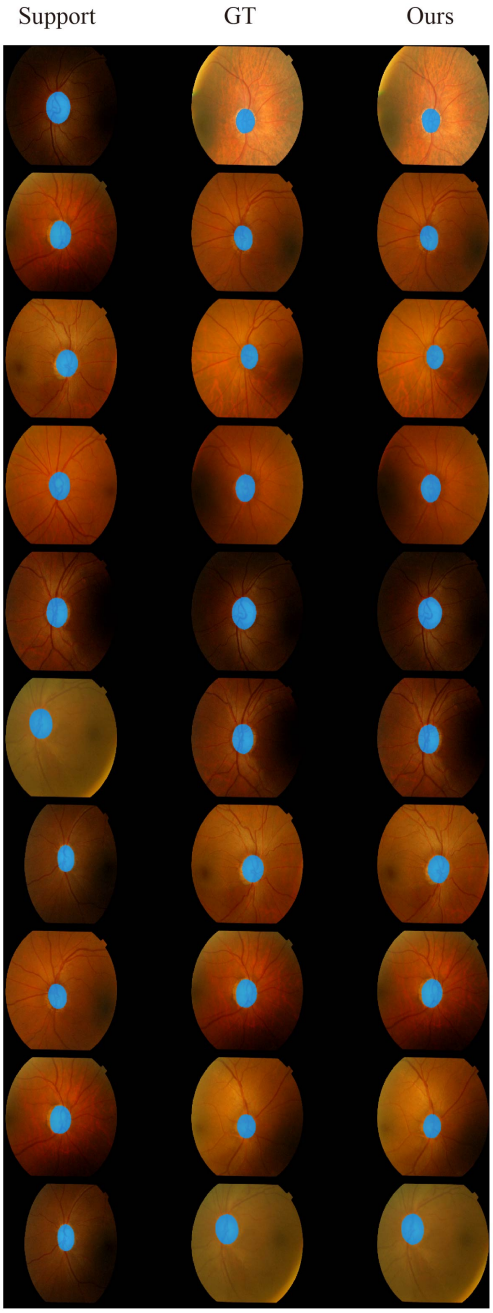

Figure 3. Visualization from left to right on Drishti-GS dataset. left row to right: Support, Ground-truth. Ours prediction.

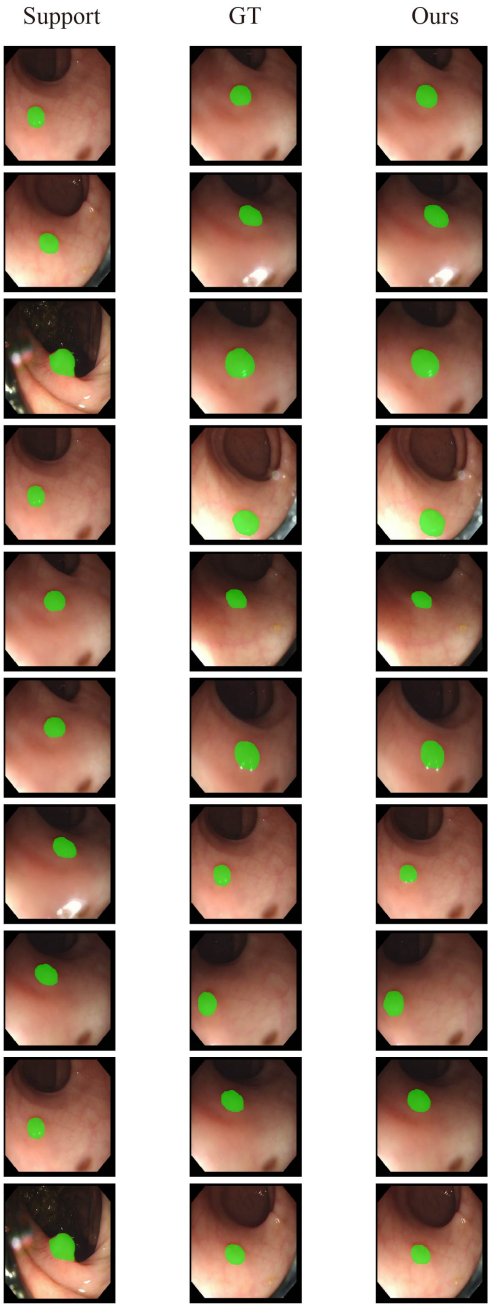

Figure 4. Visualization from left to right on CVC300 dataset. left row to right: Support, Ground-truth. Ours prediction.

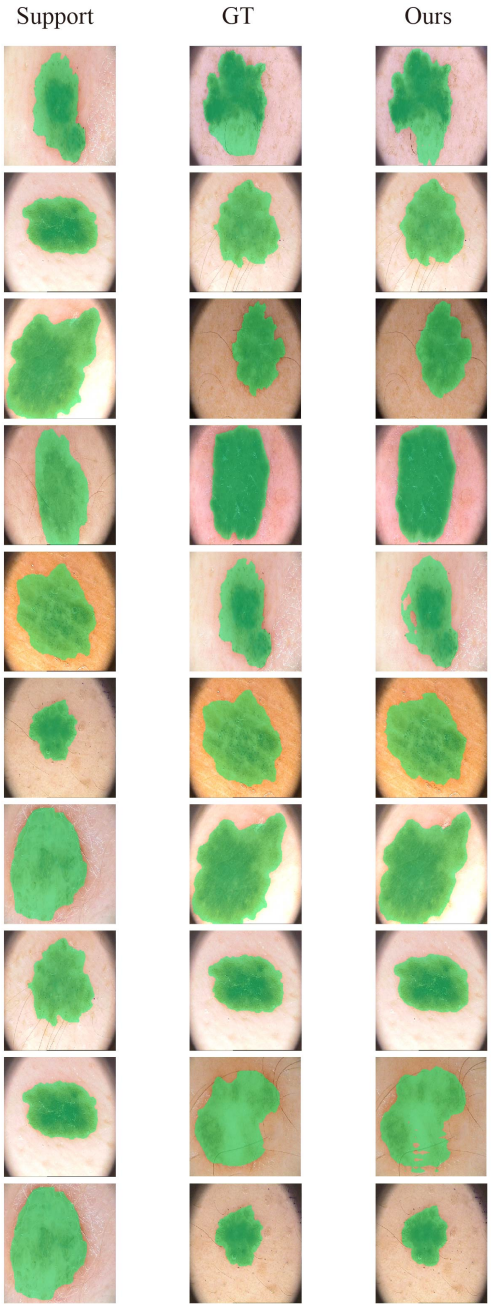

Figure 5. Visualization from left to right on PH2-typical Nevus dataset. left row to right: Support, Ground-truth. Ours prediction.

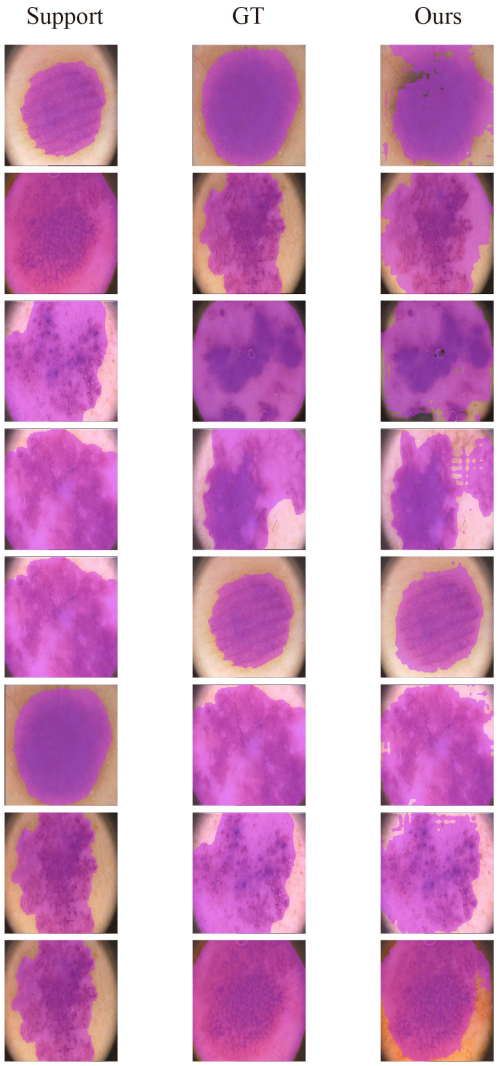

Figure 6. Visualization from left to right on PH2-Melanomas dataset. left row to right: Support, Ground-truth. Ours prediction.

References

[1] Olivier Bernard, Alain Lalande, Clement Zotti, Frederick Cervenansky, Xin Yang, Pheng-Ann Heng, Irem Cetin, Karim Lekadir, Oscar Camara, Miguel Angel Gonzalez Ballester, Gerard Sanroma, Sandy Napel, Steffen Petersen, Georgios Tziritas, Elias Grinias, Mahendra Khened, Varghese Alex Kollerathu, Ganapathy Krishnamurthi, Marc-Michel Rohe, Xavier Pennec, Maxime Sermesant, Fabian Isensee, Paul Jager, Klaus H Maier-Hein, Peter M Full, Ivo Wolf, Sandy Engelhardt, Christian F Baumgartner, Lisa M Koch, Jelmer M Wolterink, Ivana Isgum, Yeonggul Jang, Yoonmi Hong, Jay Patravali, Shubham Jain, Olivier Humbert, and Pierre-Marc Jodoin. Deep learning techniques for automatic mri cardiac multi-structures segmentation and diagnosis: Is the problem solved? *IEEE Transactions on Medical Imaging*, 37(11):2514–2525, 2018.

[2] Fernando Cervantes-Sanchez, Ivan Cruz-Aceves, Arturo Hernandez-Aguirre, Martha Alicia Hernandez-Gonzalez, and Sergio Eduardo Solorio-Meza. Automatic segmentation of coronary arteries in x-ray angiograms using multiscale analysis and artificial neural networks. *Applied Sciences*, 9(24), 2019.

[3] Muhammad Moazam Fraz, Paolo Remagnino, Andreas Hoppe, Bunyarit Uyyanonvara, Alicja R. Rudnicka, Christopher G. Owen, and Sarah A. Barman. Chase db1: Retinal vessel reference dataset. 2012.

[4] A. Emre Kavur, N. Sinem Gezer, Mustafa Barış, Sinem Aslan, Pierre-Henri Conze, Vladimir Groza, Duc Duy Pham, Soumick Chatterjee, Philipp Ernst, Savaş Özkan, Bora Baydar, Dmitry Lachinov, Shuo Han, Josef Pauli, Fabian Isensee, Matthias Perkonigg, Rachana Sathish, Ronnie Rajan, Debdoot Sheet, Gurbandurdy Dovletov, Oliver Speck, Andreas Nürnberger, Klaus H. Maier-Hein, Gözde Bozdağı Akar, Gözde Ünal, Oğuz Dicle, and M. Alper Selver. CHAOS Challenge - combined (CT-MR) healthy abdominal organ segmentation. *Medical Image Analysis*, 69:101950, 2021.

[5] Bennett Landman, Zhoubing Xu, Juan Eugenio Igelsias, Martin Styner, Thomas Robin Langerak, and Arno Klein. Miccai multi-atlas labeling beyond the cranial vault–workshop and challenge. In *Proc. of the MICCAI Multi-Atlas Labeling Beyond Cranial Vault—Workshop Challenge*, page 12, 2015.

[6] Teresa Mendonça, Pedro M. Ferreira, Jorge S. Marques, André R. S. Marcal, and Jorge Rozeira. Ph2 - a dermoscopic image database for research and benchmarking. In *2013 35th Annual International Conference of the IEEE Engineering in Medicine and Biology Society (EMBC)*, pages 5437–5440, 2013.

[7] Jayanthi Sivaswamy, S. R. Krishnadas, Gopal Datt Joshi, Madhulika Jain, and A. Ujjwaft Syed Tabish. Drishti-gs: Retinal image dataset for optic nerve head(onh) segmentation. In *2014 IEEE 11th International Symposium on Biomedical Imaging (ISBI)*, pages 53–56, 2014.

[8] David Vázquez, Jorge Bernal, Francisco Javier Sánchez, Glòria Fernández-Esparrach, Antonio M López, Adriana Romero, Michal Drozdzal, and Aaron Courville. A benchmark for endoluminal scene segmentation of colonoscopy images. *Journal of Healthcare Engineering*, 2017:4037190, 2017.